Applied Physics Reviews ARTICLE pubs.aip.org/aip/are

Ultra-sensitive microwave magnetometry with organic-molecular sensors

Cite as: Appl. Phys. Rev. **13**, 011403 (2026); doi: 10.1063/5.0271776
Submitted: 19 March 2025 · Accepted: 22 December 2025 ·
Published Online: 5 January 2026

Yuchen Han,[1] Hongliang Wu,[1,2] Hao Wu,[1] Mark Oxborrow,[3] Weibin Li,[4] Yeliang Wang,[2,5] Dezhi Zheng,[6] Dmitry Budker,[7,8,9,a)] Bo Zhang,[1,6,b)] and Jun Zhang[6,c)]

AFFILIATIONS

[1]Key Laboratory of Advanced Optoelectronic Quantum Architecture and Measurements of Ministry of Education, Center for Interdisciplinary Science of Optical Quantum and NEMS Integration, School of Physics, Beijing Institute of Technology, Beijing 100081, China
[2]School of Integrated Circuits and Electronics, Beijing Institute of Technology, Beijing 100081, China
[3]Department of Materials, Imperial College London, South Kensington, SW7 2AZ London, United Kingdom
[4]School of Physics and Astronomy, and Centre for the Mathematics and Theoretical Physics of Quantum Non-equilibrium Systems, The University of Nottingham, Nottingham NG7 2RD, United Kingdom
[5]MIIT Key Laboratory for Low-Dimensional Quantum Structure and Devices, Beijing Institute of Technology, Beijing 100081, China
[6]MIIT Key Laboratory of Complex-field Intelligent Exploration, Beijing Institute of Technology, Beijing, China
[7]Johannes Gutenberg-Universität Mainz, 55128 Mainz, Germany
[8]Helmholtz-Institut, GSI Helmholtzzentrum für Schwerionenforschung, 55128 Mainz, Germany
[9]Department of Physics, University of California, Berkeley, California 94720, USA

Note: This paper is part of the APR Special Topic on Quantum Sensing.
[a)]**Electronic mail:** budker@uni-mainz.de
[b)]**Author to whom correspondence should be addressed:** bozhang_quantum@bit.edu.cn
[c)]**Electronic mail:** zhjun@bit.edu.cn

ABSTRACT

Ultra-sensitive microwave sensing is widely demanded in various fields, ranging from cosmology to microwave quantum technology. Quantum magnetometers based on inorganic solid-state spin systems are promising for this because of their stability and biocompatibility, but the sensitivity is currently limited to a few pT/$\sqrt{\text{Hz}}$. Here, by utilizing an enhanced readout scheme with state-of-the-art solid-state maser technology, we develop a robust microwave quantum magnetometer based on spins in organic molecules at ambient conditions. Owing to the maser amplification, the sensitivity of the magnetometer reaches 6.1(2) fT/$\sqrt{\text{Hz}}$, which is three orders of magnitude better than that of the inorganic solid-state quantum magnetometers. Heterodyne detection without additional local oscillators improves the bandwidth of the sensors and allows determination of the field frequency. The scheme can be extended to other solid-state spin systems without complicated control pulses and thus enables applications, such as electron spin resonance spectroscopy, dark matter searches, and astronomical observations.

I. INTRODUCTION

Quantum sensing uses coherent and precisely controlled quantum systems to detect weak signals with unparalleled sensitivity and precision.[1] Most recently, color centers in semiconductors, for example, nitrogen-vacancy (NV) centers in diamond[2–5] have been developed as platforms for sensitive detection of microwave (MW) magnetic fields[6–9] with advantages over other systems in terms of robustness,[10] biocompatibility,[11] and spatial resolution.[12] A typical approach to improve sensitivity is to increase the number N of sensing spins, because projection noise is inversely proportional to $\sqrt{N}$.[12] However, at high spin densities, the paramagnetic impurities become a sizable source of spin dephasing, such as P1 centers in diamond,[13,14] limiting

the sensitivity of the sensors. For MW field sensing, the requirement of applying sophisticated control pulses also limits the available N.[9]

Here, we present a novel approach to sensitive MW magnetic-field detection, exploiting molecular electron spins in an organic crystal as quantum sensors. We focus on spins associated with photoexcited triplets of pentacene molecules doped in an organic single crystal when coupled to an electromagnetic mode of a microwave resonator [Fig. 1(a)], because they can be optically polarized and detected with the maser technique, and exhibit excellent coherence properties even at room temperature.[15,16] This hybrid spin-cavity quantum device can be used for room temperature maser action,[17] strong spin-photon coupling,[18] and dc-magnetometry.[19] In what follows, we show that such a system can also be used for sensing microwave magnetic fields without complicated control pulses.

We discuss two merits of such hybrid quantum sensors. First, by exploiting the stimulated emission (i.e., the masing process) of the pentacene triplet spins, which resonantly interact with the incoming microwave magnetic fields, the detected microwave signals undergo quantum amplification by up to 17 dB so that we boost the sensitivity of the sensor to 6.1(2) fT/$\sqrt{\text{Hz}}$, which is significantly better than the sensitivity of microwave quantum magnetometers based on NV centers.[6,20] Second, the cavity quantum electrodynamic (cQED) masing process enables "local-oscillator-free" heterodyne detection of the microwave signals detuned from the cavity resonance, boosting the detection bandwidth [Fig. 1(a)]. Additionally, in the absence of paramagnetic impurities, large (centimeter scale) high-density organic molecular crystals can be grown at low cost, where the sensitivity of the molecular magnetometer can be substantially improved with scaling of the number of molecular sensors $1/\sqrt{N}$.

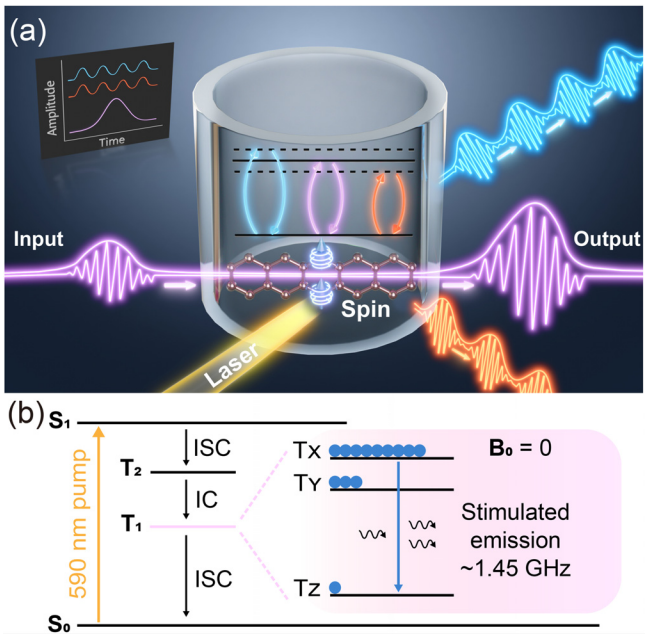

FIG. 1. The principle of a microwave quantum sensor. (a) Schematic depiction of the microwave quantum sensor. A pentacene-doped *p*-terphenyl crystal is housed within a hollow cylinder of STO. Depending on the frequency of the incident microwaves, stimulated emission occurs under resonant (purple) or off-resonant (blue and orange) conditions, generating amplified or amplitude-modulated output signals. The inset demonstrates the typical outputs of the sensor. See text for details. (b) Jablonski diagram of the spin energy level structure of the pentacene molecules doped in *p*-terphenyl. Upon excitation, highly spin-polarized states are formed with population inversion between the triplet sublevels T_X and T_Z. The input of 1.45 GHz microwave signals can trigger stimulated emission, resulting in microwave amplification.

II. RESULTS AND DISCUSSION

A. Molecular spin-based hybrid quantum system

Our quantum sensor for microwave fields is a solid-state hybrid system, in which an optically addressed molecular spin ensemble is coupled to the $TE_{01\delta}$ mode of a three-dimensional dielectric microwave cavity.[21] The spin ensemble consists of spin-triplet pentacene molecules doped in the crystalline matrix of *p*-terphenyl.[22] The pentacene molecules possess a spin magnetic moment and are inherently sensitive to a magnetic field. This makes them suitable for measuring the magnetic field components of electromagnetic fields.

As shown in Fig. 1(b), under optical pumping at a wavelength of 590 nm, the electronic spins of the pentacene molecules are promoted from the singlet ground state S_0 to the singlet excited state S_1, and then undergo transitions to the triplet state T_1 with spin selectivity through intersystem crossing (ISC) and internal conversion (IC), successively. In the geomagnetic environment (earth-field), the whole process results in a non-Boltzmann distribution of populations in the non-degenerate sublevels of T_1 at room temperature, where the population ratio of T_X:T_Y:T_Z is 0.76:0.16:0.08.[23] T_X and T_Z thus constitute an inverted two-level system with a transition frequency around 1.45 GHz. By resonantly coupling the pentacene molecules to the $TE_{01\delta}$ mode of a high-Purcell-factor microwave cavity, which is made of crystalline strontium titanate (STO),[24] a molecular spin-based hybrid quantum system is established and capable of sensitive microwave detection via measuring the magnetic field strengths of incident microwaves. The high sensitivity is achieved due to the intriguing feature of the hybrid quantum system that the received microwave photons are not only efficiently *stored* in the cavity with a high quality factor Q, but also substantially *amplified* via the stimulated emission of radiation, i.e., the masing process, between T_X and T_Z.

B. Calibration of microwave magnetic field strengths

In order to evaluate the magnetometer sensitivity, we first calibrated the sensor by applying magnetic fields of known microwave powers. A schematic of the experimental setup is shown in Fig. S3 of the supplementary material. The test fields were produced with a microwave source whose output was controlled with a microwave switch synchronized to a laser with transistor-transistor logic (TTL) pulses from an arbitrary signal generator (ASG). The strength of the test magnetic field B_1 can be varied by adjusting the input microwave power to the cavity P_{MW} with the microwave source and the variable attenuator in the circuit. The correlation between microwave power and magnetic field can be quantified by a conversion factor $C = B_1/\sqrt{P_{MW}}$,[25] which is necessary to calibrate the test fields.

The conversion factor is theoretically determined as $C = \sqrt{\frac{2\mu_0 Q_L}{V_m \omega_0}}$,[25] where $\mu_0 = 4\pi \times 10^{-7}$ H/m is the vacuum permeability, Q_L, V_m, and ω_0 are the loaded quality factor, magnetic mode

volume, and resonant frequency of the microwave cavity, respectively. The definition of the conversion factor indicates that C can be predicted by characterizing the microwave cavity employed in our sensor. The loaded quality factor of the cavity resonant at $\omega_c = 2\pi \times 1.4494$ GHz was measured to be $Q_L = 1706$ via the transmission method. The magnetic mode volume $V_m \approx 5.4 \times 10^{-7}\text{m}^3$ was determined by means of the two-dimensional (2D)-axisymmetric finite-element simulation.[26] Thus, the conversion factor C can be calculated to be $0.94\,\text{mT}/\sqrt{\text{W}}$.

By measuring the transient electron paramagnetic resonance (trEPR) on the pentacene triplet spin ensemble, the conversion factor is experimentally measured according to the frequency of the B_1-induced Rabi oscillation Ω_{Rabi},[27] as shown in Fig. 2(a) (the impact of ring-up and ring-down time is discussed in materials and methods). Based on $\Omega_{\text{Rabi}} = -\gamma_e B_1/\sqrt{2}$,[6] where $\gamma_e = -28$ MHz/mT is the gyromagnetic ratio of the electron spin (as for the pentacene triplet), the Rabi frequencies $\Omega_{\text{Rabi}} = -\gamma_e C\sqrt{P_{\text{MW}}}/\sqrt{2}$ reveal a linear correlation with the square root of the input microwave power of the cavity, and the conversion factor can be determined from the slope. The observed Rabi frequency as a function of the input microwave power in the trEPR experiment is shown in Fig. 2(b). The expected linear correlation is verified with the conversion factor $C = 1.05(3)\,\text{mT}/\sqrt{\text{W}}$, which is close to the calculated value based on the parameters of the cavity.

C. Sensitivity of the microwave quantum sensor

The sensitivity of the microwave quantum sensor was evaluated by employing an experimental setup similar to that of the trEPR measurements. The key differences were the optical pump power and the condition of the microwave cavity optimized for the masing process, thus boosting the sensor sensitivity. The optimized maser amplification was achieved when Q_L was increased from 1706 to 1857, and the cavity resonance was tuned to $\omega_c = 2\pi \times 1.4492$ GHz. It is worth noting that higher Q_L should be avoided as it would result in maser oscillations that smear the microwave signals to be detected and thus are detrimental to the sensor performance. According to the relationship $C \propto \sqrt{Q_L/\omega_c}$ validated in the trEPR experiment, the conversion factor C was slightly modified to be $1.10(3)\,\text{mT}/\sqrt{\text{W}}$ for analyzing the sensitivity.

By confirming the conversion factor, the sensitivity can be determined from the response of the sensor to a calibrated B_1 fields along with the measured noise. A series of microwave signals with different powers was input into the sensor; the corresponding B_1 fields are shown in Fig. 2(c). The response of the sensor S [Fig. 3(a)] shows a nonlinear growth with increased B_1 fields. Owing to the maser amplification, even for an nT-level weak B_1 field, it can be substantially enhanced and easily detected by the sensor in a single-shot measurement with a high signal-to-noise ratio (SNR), which is revealed by the small error bars in Fig. 3(a). The feature of the maser amplification was characterized in terms of its gain as a function of frequency, shown in the inset of Fig. 3(a). Upon sweeping the frequency of the input microwave signals ω_{in}, the cavity resonance was kept to be $\omega_c = \omega_{\text{in}}$ with the same coupling coefficient so that the B_1 fields of the input signals were kept identical (~ 50 nT) over the sweep range. The maximum gain was found to be 17 dB when $\omega_{\text{in}} = 2\pi \times 1.4492$ GHz. The distribution of the gain at different frequencies follows the inhomogeneously broadened asymmetric EPR line shape of the pentacene triplet spin ensemble, which arises from the second-order hyperfine

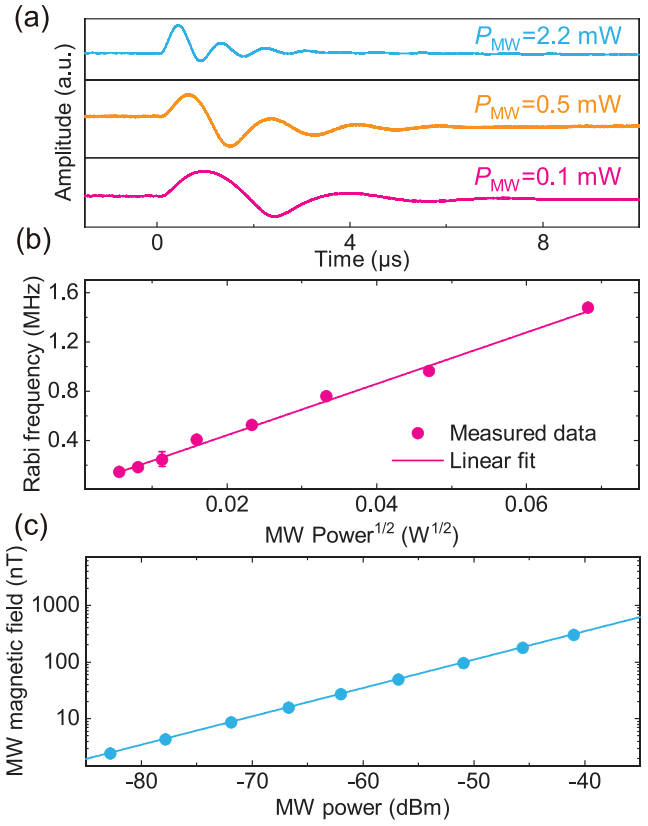

FIG. 2. Magnetic field calibration. (a) Rabi oscillation at different power levels. (b) The obtained Rabi frequencies show a linear relationship with the square roots of the power. A slope of $20.86\,\text{MHz}/\sqrt{\text{W}}$ and a microwave magnetic-field conversion factor C of $1.05\,\text{mT}/\sqrt{\text{W}}$ can be derived. Each data point represents the mean ± standard deviation obtained by repeating three individual experiments. (c) The obtained conversion factor C can be used to determine the microwave magnetic field strength at different power levels. The blue line represents the calculated relationship between the magnetic field and power, while the blue dots correspond to the power points measured in the experiment. Error bars are contained within the data points.

interactions at the earth-field.[19] The negative gain, i.e., attenuation, observed on the wings of the distribution is due to the fact that the pentacene spin subensembles far from the EPR resonance are insufficient to produce enough gain to compensate the microwave losses (see the supplementary material for the gain and frequency analysis). As shown in Fig. 3(a), the output signal is gradually saturated as the input microwave field increases, revealing that the sensor has the functionality of a limiter to protect the back-end from overload.

By differentiating the response of the sensor to B_1, the corresponding responsivity $r = \partial S/\partial B_1$ is obtained and shown in Fig. 3(b). Relying on the definition of the sensitivity, $\eta = \frac{\sigma_s}{r\sqrt{2\Delta f}}$,[19,28] in which σ_s is the standard deviation of noise in a single measurement and $\Delta f = 500$ MHz is the equivalent noise bandwidth of our data acquisition. Thus, the sensitivities under different microwave magnetic fields are determined, as depicted in Fig. 3(b); the optimal sensitivity is $1.2(2)\,\text{fT}/\sqrt{\text{Hz}}$. This is *three* orders of magnitude better than those

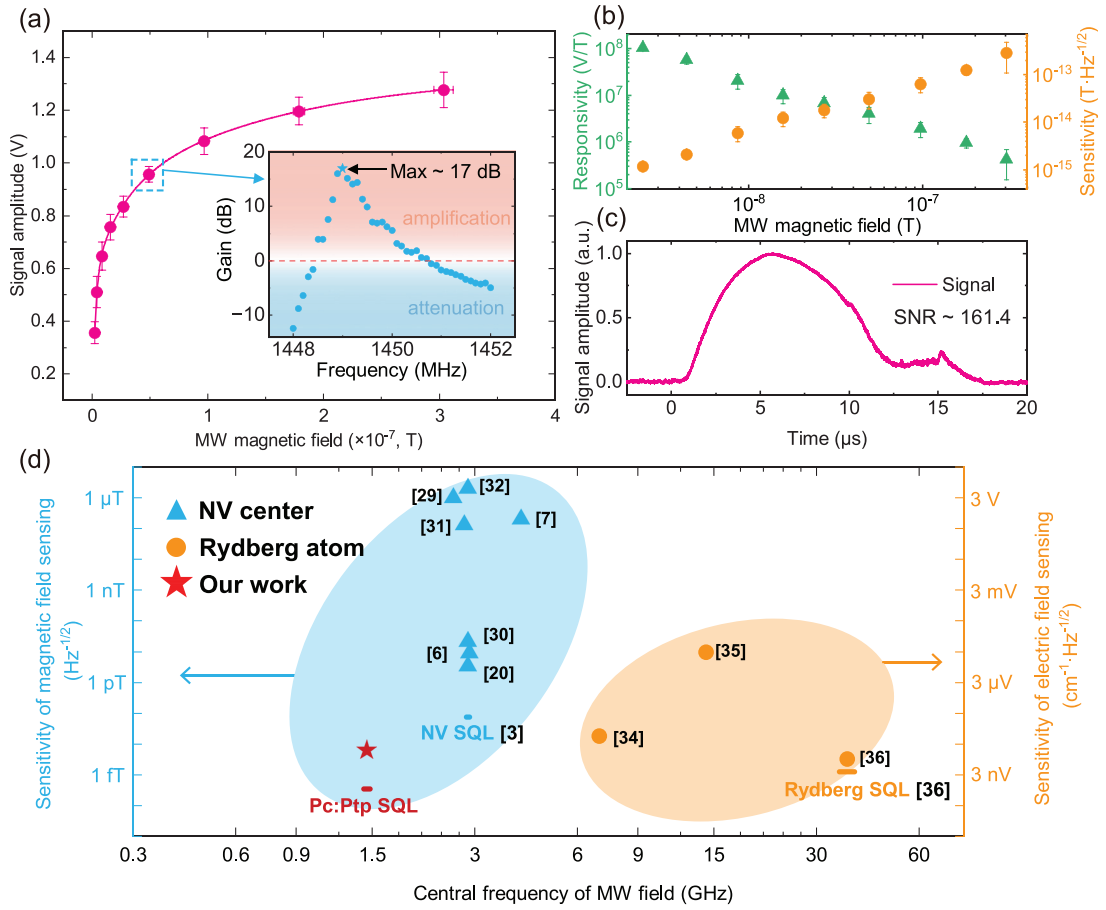

FIG. 3. The sensitivity of the microwave quantum sensor. (a) The data points represent the signal strengths measured at different microwave magnetic fields and are fitted by an exponential equation. Inset: maser amplification gain obtained at different frequencies with an input microwave magnetic-field strength of 49.23 nT. (b) Sensor responsivity (green triangles) at different magnetic fields determined from the slopes of the fitting curve in (a). The corresponding sensitivity at different magnetic fields is represented with yellow circles. The error bars represent the standard errors of the data points in (a) and (b). (c) A signal waveform with an SNR of 161.4 was obtained at the lowest input microwave magnetic field corresponding to the lowest data point in (a). (d). Comparison of the sensitivities of different microwave quantum sensors. The blue area represents the magnetic-field sensing (NV centers and pentacene doped in p-terphenyl, Pc:Ptp), whereas the yellow area represents the electric-field sensing (Rydberg atoms). The three colored lines represent the SQLs (see supplementary material Sec. S4) of Pc:Ptp (red), NV centers (blue), and Rydberg atoms (yellow), respectively. The sensitivities of the magnetometry and electrometry marked on the y-axes are mutually equivalent.

achieved with NV sensors in diamond.[6,20] We further verify the measured sensitivity by analyzing the sensor response to a weak microwave pulse with a frequency of $2\pi \times 1.4492$ GHz tuned to the peak of the cavity resonance and a field strength B_{test} of 2.47 nT [Fig. 3(c)]. We note that because of the ring-up/down time of the cavity, the input microwave signal was not only amplified but also prolonged. We obtain the SNR of the microwave power to be SNR_P=161.4, which leads to the magnetic field SNR_B=12.7. Consequently, the experimental sensitivity $(6.1(2)\,\text{fT}/\sqrt{\text{Hz}})$ of the sensor is obtained via $\eta = \frac{B_{\text{test}}}{\text{SNR}\sqrt{2\Delta f}}$,[6] which is on the same order of magnitude as the sensitivity predicted above based on the responsivity. Comparing with the reported microwave quantum sensors/magnetometers summarized in Fig. 3(d), the sensitivity of our device is superior to those of the NV-center based microwave magnetometers[6,7,20,29–33] and thus can be considered a promising room-temperature solid-state quantum device for microwave detection. On the other hand, we are also approaching the sensitivity recently achieved by cold Rydberg atoms[34–36] while revealing the robustness and integration capability in contrast to gaseous Rydberg systems.

D. Enhanced sensing via the self-frequency-mixing effect

The aforementioned microwave detection with our sensor was implemented under a resonant condition, i.e., $\omega_{\text{in}} = \omega_{\text{c}}$, while for practical sensors, the resonant condition is not always fulfilled. Therefore, it is necessary to evaluate the performance of the sensor for off-resonant microwave signals. We measured various microwaves applied to the sensor that were set between 1.4454 and 1.4534 GHz in steps of 100 kHz. Note that during our measurements, the cavity remained resonant with the broad pentacene triplet spin resonance. As

we adjusted the input frequency detuning from the cavity resonance, beatings appeared in the output of the sensor. We have experimentally confirmed that the above phenomenon is a quantum effect rather than attributed to interference between the reflected and leaked signals, because beats are only visible when the laser is on, indicating that spins must play a role in generating these signals. When detuning increased, the frequency of the beats increased linearly while the output amplitude was reduced, as shown in Figs. 4(a) and 4(b). The decreased amplitude arose from (i) the lower maser gain at off resonance, as demonstrated in the inset of Fig. 3(a); (ii) the loss of the detected signal due to detuning-induced reflection at the cavity input port, which was characterized through the $S-$ parameter measurement (see the supplementary material). The beat frequency is equal to the detuning $\Delta\omega = \omega_c - \omega_{in}$.

The measured beat frequency agrees with the theoretical prediction (see supplementary material for details), as shown in Fig. 4(a), which reveals that our quantum sensor is also capable of heterodyne measurements. More intriguingly, different from the reported

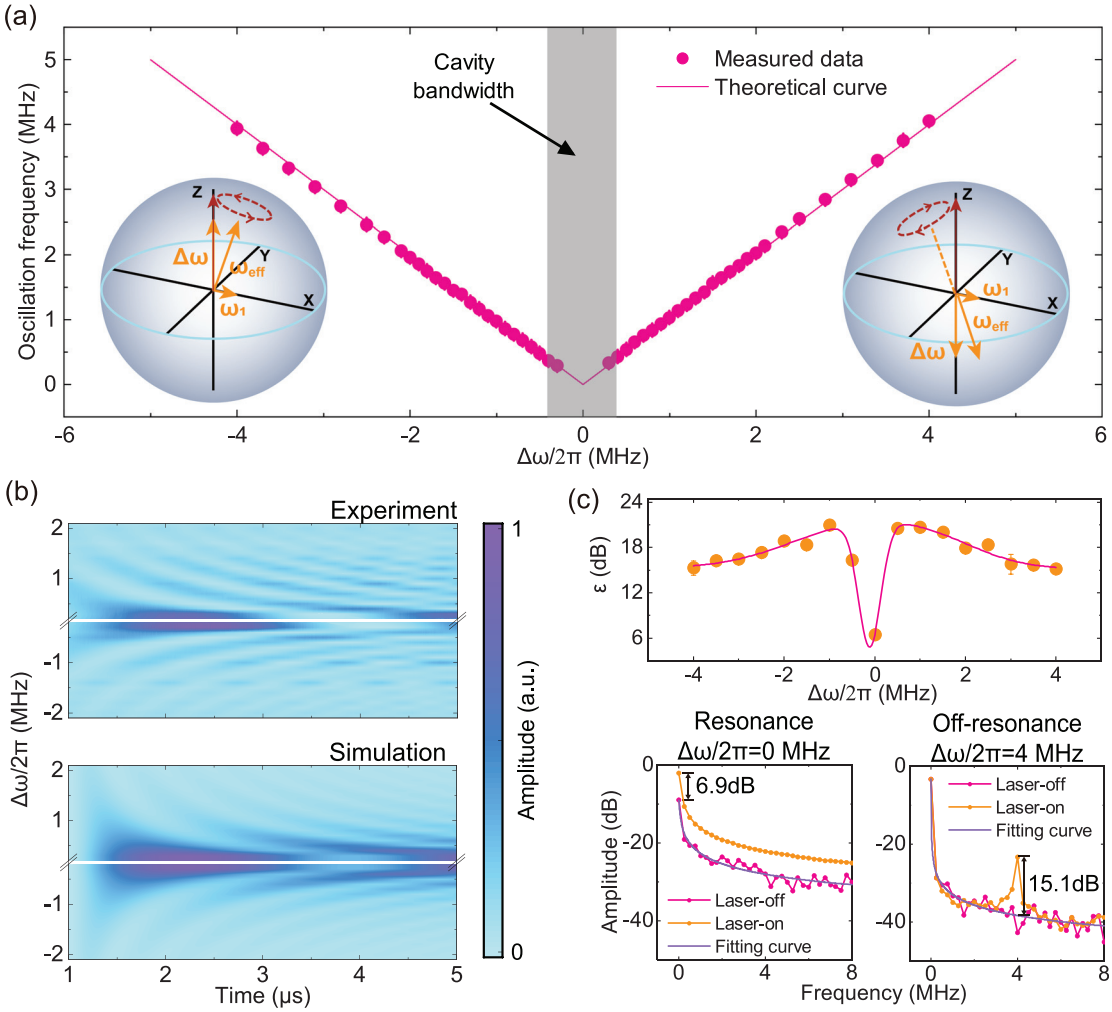

FIG. 4. Proof-of-principle demonstrations of heterodyne detection of microwave fields. (a) The beats between the frequency of the cavity resonant mode $\omega_c = 2\pi \times 1.4494$ GHz, and the detuned input microwaves are mapped out with respect to the detuning frequency $\Delta\omega$. A linear relationship is displayed with a frequency range of ± 4 MHz, which is far beyond the bandwidth of the cavity (~ 800 kHz). The error bars are contained within the data points. Inset: two Bloch spheres qualitatively describe the oscillations of polarized spin under negative (left) and positive (right) detunings. The three orange arrows represent the equivalent magnetic field of the input microwaves in the rotating frame, including the detuning frequency ($\Delta\omega$), the Rabi frequency (ω_1) induced by the B_1 field, and their vector sum (ω_{eff}). The red arrow represents the polarized spin, pointing from the origin toward the positive direction of the z-axis. It undergoes Larmor precession around the axis ω_{eff}, and the red dashed arrow with an arrowhead indicates the direction of the precession. (b) The experimental and simulated maser response under varying detuning frequency of the off-resonant microwave fields. The beatings with different detunings are mapped out as a function of time after applying laser pulses (upper) while the dynamics are simulated based on the driven Tavis–Cummings model (lower), see materials and methods. (c) The upper subplot represents the enhancement figure-of-merit of heterodyne detection of microwave field sensing. The bottom left and right subplots represent the FFT results for signals of laser-on (yellow) and -off (pink) under resonance (left) and off resonance (right), respectively. The purple line gives the fitted curve of the FFT data (pink) when the laser is off. The data points represent the mean $\pm$ standard deviation obtained from five experiments.

quantum sensors, i.e., NV centers[6,37] and Rydberg atoms[34] that employ classical microwave sources for the local oscillators of heterodyne measurements, our hybrid quantum system by itself acts like the local oscillator for frequency mixing. The underlying physics is the self-frequency-mixing effect between an off-resonant microwave field and the pentacene triplet spin ensemble, which can be described by the driven Tavis–Cummings model[38,39] (see materials and methods for details), while the equality of the beat frequency detuning can be explained by solving Maxwell–Bloch equations,[40] see supplementary material.

In terms of the detection of the input frequency, since the duration of the input microwaves in our measurements was 5 μs limited by the duration of masing, the frequency of the beats is unresolvable unless it is larger than about 200 kHz, whereas those signals with detuning smaller than 200 kHz can be observed with a prominent amplification near resonance. Despite the presence of the cavity playing the role of a narrow-band filter, our detection range was not limited by the cavity bandwidth ($\approx$ 800 kHz). Strikingly, the detuning range where the beats can be observed exceeds the cavity bandwidth by approximately an order of magnitude, i.e., $\pm$ 4 MHz. In principle, the beat-frequency range could be broader (about $\pm$10 MHz[19]), where the magnetic resonance of the pentacene triplet spin ensemble is measurable, i.e., a sufficient number of spins are present in the range of the input frequency.

As the incident microwaves are measured by observing the output power of the maser-amplified signal, i.e., the maser-burst envelope, which is measured directly by a logarithm detector, the modulated oscillations of the envelopes resulting from the self-frequency-mixing effects circumvent the $1/f$ noise in contrast to the resonant detection yielding near-DC signals. To verify this, we introduce a figure of merit, ε to compare the on- and off-resonance detection enhancement offered by the sensor. ε was obtained from the ratio between the fast Fourier transform (FFT) amplitudes measured with and without the laser excitation, i.e., the sensor was switched on and off (see Sec. IV). As shown in Fig. 4(c), compared with the resonant detection, the heterodyne detection under the detuning conditions is improved, and the enhancement of $\varepsilon = 15.1$ dB was achieved at $\Delta\omega/2\pi = 4$ MHz, whereas ε obtained on resonance was 8.9 dB lower. The above experimental results indicate that, while the maser signal gain was reduced in the detuned case compared to the resonant case, it also lowers the noise floor by reducing the $1/f$ noise, leading to an overall improvement in SNR. A higher SNR enhancement means that weaker signals can be detected more effectively compared to the resonance condition, resulting in better sensitivity. In addition, we found that although ε measured at $\Delta\omega > 0$ and $\Delta\omega < 0$ is largely symmetrical, the part with $\Delta\omega > 0$ is slightly larger overall than the part with $\Delta\omega < 0$, and the downward trend is slower, with a slightly larger half-width. This was attributed to the asymmetric EPR line shape of the pentacene triplet spin ensemble in which the spin subensembles are distributed preferentially in the regime $\Delta\omega > 0$ rather than $\Delta\omega < 0$ due to the second-order hyperfine interactions.[41] Although the self-frequency-mixing-effect-assisted sensor possesses similar features to the heterodyne detectors, i.e., high sensitivity and the detected signals originate from the frequency beating, our approach effectively expands the detection bandwidth, especially lifts the restriction of the setup by the cavity, whereas the traditional heterodyne technique sacrifices the detection bandwidth for the sensitivity.

III. CONCLUSION

We have demonstrated a microwave quantum sensor based on the pentacene triplet spin ensemble coupled to a microwave cavity at ambient conditions. The detection scheme of the sensor is to measure microwave *magnetic* fields, in contrast to the traditional $\lambda/2$ dipole antennas and the Rydberg atomic sensors, which are essentially electrometers. By exploiting the maser amplification in the solid-state hybrid quantum system at about 1.45 GHz, the sensor sensitivity of $6.14(17)\,\mathrm{fT}/\sqrt{\mathrm{Hz}}$ is achieved. This figure surpasses the state-of-the-art microwave magnetometers based on solid-state spins of NV centers,[6,20] and can be further improved by reducing the system noise temperature. Under our current system at room temperature, the noise temperature can be roughly estimated to be 99 K (see the supplementary material), which can be further reduced by increasing the maser gain, reducing the loss caused by the circulator and signal transmission.[17] Moreover, the self-frequency-mixing effects in the hybrid quantum system enable us to detect microwave signals outside the cavity bandwidth by monitoring the heterodyne-like frequency beats with high SNR. Using the beats removes the restriction of the detection bandwidth set by the cavity and offers enhanced detection capability under large-detuning conditions compared to the resonant scenarios. Unlike the heterodyne measurements demonstrated using the Rydberg atoms and NV centers that often require an external source to provide a local microwave field, our sensor operates without the need for such external microwave sources, which renders unique advantages, e.g., convenience and simplicity.

Our device, possessing both functionalities of quantum mixers and amplifiers, expands the quantum toolbox for ultrahigh-sensitivity microwave detection and provides promising approaches for improving current microwave receiver systems in radars,[42] wireless communications,[43] radio telescopes,[44] microwave circuitry imaging,[45] and ESR/EPR.[25,40] Our scheme, incorporating the amplification characteristic of masers in the sensing of microwave fields, can be extended to various mature solid-spin quantum systems, e.g., those based on silicon vacancies in silicon carbide,[46,47] negatively charged boron vacancies in the van der Waals hexagonal boron nitride crystals,[48,49] or NV centers in diamond.[50,51] To enhance the ability of the device for the detection of continuous-wave (CW) fields, extending our scheme to a CW mode may be a solution in the future. Although CW pentacene masers have not yet been realized, significant progress in this area has been made, and the quasi-CW operation of a pentacene maser at room temperature has recently been demonstrated,[52] indicating the feasibility.

IV. MATERIALS AND METHODS

A. Experimental setup

Configured as a cavity amplifier operated in reflection through a circulator, the setup of the microwave sensor is shown in the supplementary material. By utilizing the finite-element-method software, we designed the microwave cavity, which was constructed from a hollow cylindrical single-crystal of STO containing a 0.1 % pentacene-doped *p*-terphenyl crystal (7.2 mm height, 4 mm width, 1.5 mm average thickness). The STO hollow cylinder was mounted on a Rexolite support and housed within a cylindrical copper enclosure. A copper tuning piston at the top of the cavity was used to change the distance between the STO cylinder and the ceiling of the cavity to adjust the resonant frequency of the $TE_{01\delta}$ mode. The microwave resonator was directly coupled to a circulator using a small loop antenna as an

undercoupled input/output port. By splitting the amplified microwave signals with a power splitter, we directly monitored the amplified microwave fields with a digital storage oscilloscope (Tektronix MSO64; sampling rate 6.25 GSa/s), whereas the power of the amplified microwave signals was measured with a logarithmic detector (AD8317; scale, 22 mV/dB), AC-coupled to the oscilloscope.

An optical parametric oscillator, OPO (Deyang Tech. Inc., BBOPO-Vis; pulse duration, 7 ns), pumped by its own internal Q-switched Nd:YAG laser, was used to excite the pentacene crystal. The injected pump-laser pulses, as well as the test microwave fields generated from a MW source (SynthHDPro V2), were triggered by an ASG (arbitrary sequence generator, CIQTEK, ASG8400).

B. On-resonance microwave magnetic field detection

The microwave cavity was characterized with a microwave analyzer (Keysight, N9917A, see supplementary material). The measurement setups for the trEPR, maser-gain, and microwave magnetic field detection are the same, as described above. The microwave power used for the trEPR measurement was set from −14.98 to 6.67 dBm. The laser pulse used for the measurements of trEPR, maser gain, and microwave magnetic field detection was monitored with a photodetector (Thorlabs, DET10A2).

When detecting the resonant microwave magnetic field, the maser-amplification method was adopted. There are two operating regimes for the maser: the amplification regime and the self-oscillation regime. In the amplification regime, the maser outputs a signal only when there is an input signal, whereas in the self-oscillation regime, the maser produces an oscillation signal even in the absence of an input. Our system operates in the amplification regime (the input signal to be amplified is weak, so it does not saturate the amplification process) 5 μs microwave square-wave pulse in the experiment), as confirmed by our experiments, where no self-oscillation is observed.

C. Heterodyne detection

We perform heterodyne detection with detuned microwave fields. The power of input microwaves generated by the microwave source was −56.8 dBm, and the frequency was varied from 1.4454 to 1.4534 GHz. To verify that heterodyne detection can circumvent the $1/f$ noise, we introduced an enhancement figure of merit defined as

$$\varepsilon = \left.\frac{\mathrm{FFT(LaserON)}}{\mathrm{FFT(LaserOFF)}}\right|_{\Delta\omega}. \tag{1}$$

In Eq. (1), the numerator is the FFT of the output signal at $\Delta\omega$ when there is a detuned signal input and the laser is turned on, while the denominator is obtained through curve fitting under the condition that the laser is turned off (with the input detuned signal applied). When the laser is turned off, we still perform an FFT on the output signal. We fitted the FFT spectrum using the function $y = 10\lg(a/(f+b)^c)$, where a, b, and c are fitting parameters, and y represents the spectral density of signal amplitude (expressed in dB).

We note that ε is not the SNR, however, it positively correlates with the improvement of SNR brought by the maser process. Comparing the "laser ON" and "laser OFF" states, the maser effect enhances the efficiency of the signal detection, which is quantified by ε.

D. Cavity electrodynamics of the maser process

To give a dynamical description of the maser process with detuning in Fig. 4, we start from the driven Tavis–Cummings Hamiltonian in the rotating frame[38,39]

$$H = \hbar\Delta_c a^\dagger a + \frac{\hbar}{2}\Delta_s\sum_{j=1}^{N}\sigma_j^z + \hbar\sum_{j=1}^{N}\left[g_j\sigma_j^- a^\dagger + g_j^*\sigma_j^+ a\right] + i\hbar[Va^\dagger - V^* a], \tag{2}$$

where $\Delta_c = \omega_c - \omega_{in}$ and $\Delta_s = \omega_s - \omega_{in}$ are the detunings of the resonator frequency ω_c and of the spin frequencies ω_s from the input frequency ω_{in} of the incoming microwave pulse with amplitude V. $a^\dagger(a)$ is the creation (annihilation) operator for the resonator mode, coupling with g_j to the jth spin that is presented wwith the Pauli operators σ_j^z, σ_j^+, and σ_j^-.

The evolution of the system can be described according to the quantum master equation, which is written as

$$\frac{\mathrm{d}\rho}{\mathrm{d}t} = -\frac{1}{i\hbar}[\rho, H] + \mathcal{L}[\rho], \tag{3}$$

where $\mathcal{L}[\rho]$ stands for the Liouvillian[18,53]

$$\mathcal{L}[\rho] = \kappa_c(a\rho a^\dagger - \frac{1}{2}(a^\dagger a\rho + \rho a^\dagger a)) + \gamma_\parallel\sum_{j=1}^{N}(\sigma_j^z\rho\sigma_j^z - \rho) + \frac{\gamma_\perp}{2}\sum_{j=1}^{N}(2\sigma_j^-\rho\sigma_j^+ - \sigma_j^+\sigma_j^-\rho - \rho\sigma_j^+\sigma_j^-) + \frac{\gamma_\perp}{2}\sum_{j=1}^{N}(2\sigma_j^+\rho\sigma_j^- - \sigma_j^-\sigma_j^+\rho - \rho\sigma_j^-\sigma_j^+). \tag{4}$$

The first term in Eq. (4) describes the cavity losses with the decay rate κ_c, the second and third terms represent the longitudinal and transversal decay with rates $\gamma_\parallel$ and $\gamma_\perp$, respectively.

In the large spin ensembles limit, correlations between the cavity mode and spins can be neglected,[39] for example, $\langle\sigma_j^+ a\rangle \approx \langle\sigma_j^+\rangle\langle a\rangle$. According to the Lindblad master Eqs. (3) and (4) and the approximate conditions above, we obtain a set of first-order differential equations for the expectation values of the cavity mode field $\langle a\rangle$ and spin angular momentum $\langle\tilde{S}_-\rangle$ and $\langle\tilde{S}_z\rangle$

$$\frac{\mathrm{d}}{\mathrm{d}t}\langle a\rangle = -\left[\frac{1}{2}\kappa_c + i\Delta_c\right]\langle a\rangle - ig_{\mathrm{eff}}\langle\tilde{S}_-\rangle + V, \tag{5}$$

$$\frac{\mathrm{d}}{\mathrm{d}t}\langle\tilde{S}_-\rangle = -\left[\frac{1}{2}\gamma_\parallel + i\Delta_s\right]\langle\tilde{S}_-\rangle + ig_{\mathrm{eff}}\frac{1}{N}\langle\tilde{S}_z\rangle\langle a\rangle, \tag{6}$$

$$\frac{\mathrm{d}}{\mathrm{d}t}\langle\tilde{S}_z\rangle = -\gamma_\perp\langle\tilde{S}_z\rangle + 2ig_{\mathrm{eff}}\frac{1}{N}(\langle\tilde{S}_-\rangle\langle a^\dagger\rangle - \langle\tilde{S}_+\rangle\langle a\rangle), \tag{7}$$

where $\tilde{S}_\pm = \frac{1}{\sqrt{N}}\sum_{j=1}^{N}\sigma_j^\pm$ and $\tilde{S}_z = \frac{1}{N}\sum_{j=1}^{N}\sigma_j^z$ are collective spin operators, and $g_{\mathrm{eff}} = g\sqrt{N}$ represents the coupling strength which is derived under an assumption that the spin–photon coupling of each spin is the same and is a real number, i.e., $g_j = g_j^* = g$ for any j. $\langle O\rangle$ is the expectation value of the operator O. Numerical solutions of the set of differential equations (5)–(7) are achieved by utilizing the Runge–Kutta method. To fit the experimental results measured by a logarithmic detector in Fig. 4(a), the simulated results shown in Fig. 4(b) were

calculated by $\lg\langle a^\dagger a\rangle$ and normalized by its maximum and minimum values. In the simulation, an approximation $\langle a^\dagger a\rangle \approx \langle a^\dagger\rangle\langle a\rangle = |\langle a\rangle|^2$ is adopted, where $\langle a\rangle$ is obtained from the solutions of Eqs. (5)–(7).

E. Ring time in Rabi frequency measurement

Rabi oscillation by using time-resolved electron paramagnetic resonance (trEPR) is a standard method for calibrating the B_1 field.[6,20]

In our system, the ring-up and ringdown times can be calculated as $\tau_R = 2Q_L/\omega_c = 1857/(1.4492\ \text{GHz} \times \pi) \approx 407.88\ \text{ns}$. In our experiment, the maximum Rabi frequency is less than 1.6 MHz, resulting in a period longer than 625 ns, which is longer than the ring-up and ringdown times. Additionally, the duration of microwave input extends up to 5 μs, which is an order of magnitude longer than the ring-up and ringdown times.

Therefore, the influence of ring-up and ringdown time is primarily concentrated in the first and last periods of the Rabi oscillation, rather than in the intermediate period, which does not affect the measurement of the Rabi frequency.

SUPPLEMENTARY MATERIAL

See the supplementary material for responsivity and sensitivity calculations (Sec. S1); relationship between gain and frequency (Sec. S2); *S*-parameter measurements and its figure (Sec. S3 and Supplementary material Fig. S1); SQL of our system (Sec. S4); qualitative analysis to enhance sensitivity (Sec. S5); parameters and initial conditions determination in the dynamics simulation (Sec. S6); modeling of the spin dynamics in heterodyne detection (Sec. S7); evaluation of noise temperature (Sec. S8); comparison of the sensitivities of different microwave quantum sensors (supplementary material Fig. S2) and the measurement setup (supplementary material Fig. S3).

ACKNOWLEDGMENTS

We thank Ya Wang for valuable discussions. This work was supported by NSF of China (Grant Nos. T2522007, 12441502, 12374462, 12004037, 91859121, 12204040, and 12321004), the National Key R&D Program of China (Grant No. 2018YFA0306600), Chinese Academy of Sciences President's International Fellowship Initiative Grant No. 2025PD0173 and the China Postdoctoral Science Foundation (Grant Nos. YJ20210035, 2021M700439, and 2023T160049), EPSRC New Horizons grant EP/V048430/1.

AUTHOR DECLARATIONS

Conflict of Interest

The authors have no conflicts to disclose.

Author Contributions

Yuchen Han, Hongliang Wu, and Hao Wu contributed equally to this work.

Yuchen Han: Conceptualization (supporting); Data curation (equal); Formal analysis (equal); Funding acquisition (equal); Investigation (equal); Methodology (equal); Supervision (equal); Visualization (equal); Writing – original draft (equal); Writing – review & editing (equal). **Hongliang Wu:** Data curation (equal); Formal analysis (equal); Funding acquisition (equal); Investigation (equal); Methodology (supporting); Supervision (equal); Visualization (equal); Writing – original draft (equal); Writing – review & editing (equal). **Hao Wu:** Conceptualization (equal); Data curation (supporting); Formal analysis (equal); Funding acquisition (supporting); Investigation (equal); Methodology (equal); Supervision (equal); Writing – original draft (equal); Writing – review & editing (supporting). **Mark Oxborrow:** Formal analysis (supporting); Funding acquisition (equal); Investigation (supporting); Resources (supporting); Writing – review & editing (equal). **Weibin Li:** Conceptualization (equal); Data curation (supporting); Formal analysis (equal); Funding acquisition (equal); Investigation (equal); Methodology (equal); Supervision (equal); Writing – original draft (equal); Writing – review & editing (equal). **Yeliang Wang:** Conceptualization (supporting); Data curation (equal); Formal analysis (equal); Funding acquisition (equal); Investigation (equal); Methodology (equal); Supervision (equal); Visualization (equal); Writing – original draft (equal). **Dezhi Zheng:** Data curation (equal); Formal analysis (equal); Funding acquisition (supporting); Investigation (equal); Methodology (supporting); Supervision (supporting); Visualization (equal); Writing – original draft (equal); Writing – review & editing (equal). **Dmitry Budker:** Formal analysis (equal); Funding acquisition (equal); Investigation (supporting); Resources (supporting); Writing – review & editing (equal). **Bo Zhang:** Conceptualization (equal); Data curation (equal); Formal analysis (equal); Funding acquisition (equal); Investigation (equal); Methodology (equal); Supervision (equal); Visualization (equal); Writing – original draft (equal); Writing – review & editing (equal). **Jun Zhang:** Supervision (equal); Writing – review & editing (equal).

DATA AVAILABILITY

The data that support the findings of this study are available within the article and its supplementary material.

REFERENCES

[1] C. L. Degen, F. Reinhard, and P. Cappellaro, "Quantum sensing," Rev. Mod. Phys. **89**, 035002 (2017).
[2] D. A. Antheunis, J. Schmidt, and J. H. van der Waals, "Spin-forbidden radiationless processes in isoelectronic molecules: Anthracene, acridine and phenazine," Mol. Phys. **27**, 1521 (1974).
[3] J. F. Barry, M. J. Turner, J. M. Schloss, D. R. Glenn, Y. Song, M. D. Lukin, H. Park, and R. L. Walsworth, "Optical magnetic detection of single-neuron action potentials using quantum defects in diamond," Proc. Natl. Acad. Sci. U. S. A. **113**, 14133 (2016).
[4] S. L. Bayliss, D. W. Laorenza, P. J. Mintun, B. D. Kovos, D. E. Freedman, and D. D. Awschalom, "Optically addressable molecular spins for quantum information processing," Science **370**, 1309 (2020).
[5] E. H. Chen, O. Gaathon, M. E. Trusheim, and D. Englund, "Wide-field multispectral super-resolution imaging using spin-dependent fluorescence in nanodiamonds," Nano Lett. **13**, 2073 (2013).
[6] Z. Wang, F. Kong, P. Zhao, Z. Huang, P. Yu, Y. Wang, F. Shi, and J. Du, "Picotesla magnetometry of microwave fields with diamond sensors," Sci. Adv. **8**, abq8158 (2022).
[7] J. Meinel, V. Vorobyov, B. Yavkin, D. Dasari, H. Sumiya, S. Onoda, J. Isoya, and J. Wrachtrup, "Heterodyne sensing of microwaves with a quantum sensor," Nat. Commun. **12**, 2737 (2021).
[8] T. Joas, A. M. Waeber, G. Braunbeck, and F. Reinhard, "Quantum sensing of weak radio-frequency signals by pulsed Mollow absorption spectroscopy," Nat. Commun. **8**, 964 (2017).
[9] A. Stark, N. Aharon, T. Unden, D. Louzon, A. Huck, A. Retzker, U. L. Andersen, and F. Jelezko, "Narrow-bandwidth sensing of high-frequency fields with continuous dynamical decoupling," Nat. Commun. **8**, 1105 (2017).

[10]G.-Q. Liu, X. Feng, N. Wang, Q. Li, and R.-B. Liu, "Coherent quantum control of nitrogen-vacancy center spins near 1000 kelvin," Nat. Commun. **10**, 1344 (2019).
[11]F. Shi, F. Kong, P. Zhao, X. Zhang, M. Chen, S. Chen, Q. Zhang, M. Wang, X. Ye, Z. Wang, Z. Qin, X. Rong, J. Su, P. Wang, P. Z. Qin, and J. Du, "Single-DNA electron spin resonance spectroscopy in aqueous solutions," Nat. Methods **15**, 697 (2018).
[12]J. M. Taylor, P. Cappellaro, L. Childress, L. Jiang, D. Budker, P. R. Hemmer, A. Yacoby, R. Walsworth, and M. D. Lukin, "High-sensitivity diamond magnetometer with nanoscale resolution," Nat. Phys. **4**, 810 (2008).
[13]R. Hanson, V. V. Dobrovitski, A. E. Feiguin, O. Gywat, and D. D. Awschalom, "Coherent dynamics of a single spin interacting with an adjustable spin bath," Science **320**, 352 (2008).
[14]F. T. Charnock and T. A. Kennedy, "Combined optical and microwave approach for performing quantum spin operations on the nitrogen-vacancy center in diamond," Phys. Rev. B **64**, 041201(R) (2001).
[15]A. Mena, S. K. Mann, A. Cowley-Semple, E. Bryan, S. Heutz, D. R. McCamey, M. Attwood, and S. L. Bayliss, "Room-temperature optically detected coherent control of molecular spins," arXiv:2402.07572 (2024).
[16]H. Singh, N. D'Souza, K. Zhong, E. Druga, J. Oshiro, B. Blankenship, J. A. Reimer, J. D. Breeze, and A. Ajoy, "Room-temperature quantum sensing with photoexcited triplet electrons in organic crystals," arXiv:2402.13898 (2024).
[17]M. Oxborrow, J. D. Breeze, and N. M. Alford, "Room-temperature solid-state maser," Nature **488**, 353 (2012).
[18]J. D. Breeze, E. Salvadori, J. Sathian, N. M. Alford, and C. W. M. Kay, "Room-temperature cavity quantum electrodynamics with strongly coupled Dicke states," npj Quantum Inf. **3**, 40 (2017).
[19]H. Wu, S. Yang, M. Oxborrow, M. Jiang, Q. Zhao, D. Budker, B. Zhang, and J. Du, "Enhanced quantum sensing with room-temperature solid-state masers," Sci. Adv. **8**, eade1613 (2022).
[20]S. T. Alsid, J. M. Schloss, M. H. Steinecker, J. F. Barry, A. C. Maccabe, G. Wang, P. Cappellaro, and D. A. Braje, "Solid-state microwave magnetometer with picotesla-level sensitivity," Phys. Rev. Appl. **19**, 054095 (2023).
[21]E. C. Liang, "An overview of high Q TE mode dielectric resonators and applications," Ph.D. thesis, Department of Electronic Engineering, University of California, Los Angeles, CA, 2015.
[22]H. Wu, "Room-temperature quantum devices based on pentacene's photo-excited triplet state in *p*-terphenyl," Ph.D. thesis (Imperial College London, 2020).
[23]D. J. Sloop, H.-L. Yu, T.-S. Lin, and S. Weissman, "Electron spin echoes of a photoexcited triplet: Pentacene in *p*-terphenyl crystals," J Chem. Phys. **75**, 3746 (1981).
[24]J. Breeze, K.-J. Tan, B. Richards, J. Sathian, M. Oxborrow, and N. M. Alford, "Enhanced magnetic Purcell effect in room-temperature masers," Nat. Commun. **6**, 6215 (2015).
[25]C. Poole, *Electron Spin Resonance: A Comprehensive Treatise on Experimental Techniques*, A Wiley-Interscience Publication (Wiley, 1983).
[26]M. Oxborrow, "Traceable 2-D finite-element simulation of the whispering-gallery modes of axisymmetric electromagnetic resonators," IEEE Trans. Microwave Theory Tech. **55**, 1209 (2007).
[27]S. Weber, *Transient EPR* (Wiley Weinheim, Germany, 2018), pp. 195–214.
[28]J. M. Schloss, J. F. Barry, M. J. Turner, and R. L. Walsworth, "Simultaneous broadband vector magnetometry using solid-state spins," Phys. Rev. Appl. **10**, 034044 (2018).
[29]P. Wang, Z. Yuan, P. Huang, X. Rong, M. Wang, X. Xu, C. Duan, C. Ju, F. Shi, and J. Du, "High-resolution vector microwave magnetometry based on solid-state spins in diamond," Nat. Commun. **6**, 6631 (2015).
[30]X.-D. Chen, E.-H. Wang, L.-K. Shan, S.-C. Zhang, C. Feng, Y. Zheng, Y. Dong, G.-C. Guo, and F.-W. Sun, "Quantum enhanced radio detection and ranging with solid spins," Nat. Commun. **14**, 1288 (2023).
[31]A. Horsley, P. Appel, J. Wolters, J. Achard, A. Tallaire, P. Maletinsky, and P. Treutlein, "Microwave device characterization using a widefield diamond microscope," Phys. Rev. Appl. **10**, 044039 (2018).
[32]X.-D. Chen, D.-F. Li, Y. Zheng, S. Li, B. Du, Y. Dong, C.-H. Dong, G.-C. Guo, and F.-W. Sun, "Superresolution multifunctional sensing with the nitrogen-vacancy center in diamond," Phys. Rev. Appl. **12**, 044039 (2019).
[33]E. R. Eisenach, J. F. Barry, M. F. O'Keeffe, J. M. Schloss, M. H. Steinecker, D. R. Englund, and D. A. Braje, "Cavity-enhanced microwave readout of a solid-state spin sensor," Nat. Commun. **12**, 1357 (2021).
[34]M. Jing, Y. Hu, J. Ma, H. Zhang, L. Zhang, L. Xiao, and S. Jia, "Atomic superheterodyne receiver based on microwave-dressed Rydberg spectroscopy," Nat. Phys. **16**, 911 (2020).
[35]J. A. Sedlacek, A. Schwettmann, H. Kübler, R. Löw, T. Pfau, and J. P. Shaffer, "Microwave electrometry with Rydberg atoms in a vapour cell using bright atomic resonances," Nat. Phys. **8**, 819 (2012).
[36]H.-T. Tu, K.-Y. Liao, G.-D. He, Y.-F. Zhu, S.-Y. Qiu, H. Jiang, W. Huang, W. Bian, H. Yan, and S.-L. Zhu, "Approaching the standard quantum limit of a Rydberg-atom microwave electrometer," arXiv:2307.15617 (2023).
[37]G. Wang, Y.-X. Liu, J. M. Schloss, S. T. Alsid, D. A. Braje, and P. Cappellaro, "Sensing of arbitrary-frequency fields using a quantum mixer," Phys. Rev. X **12**, 021061 (2022).
[38]M. Tavis and F. W. Cummings, "Exact solution for an *N*-molecule—Radiation-field Hamiltonian," Phys. Rev. **170**, 379 (1968).
[39]S. Weichselbaumer, M. Zens, C. W. Zollitsch, M. S. Brandt, S. Rotter, R. Gross, and H. Huebl, "Echo trains in pulsed electron spin resonance of a strongly coupled spin ensemble," Phys. Rev. Lett. **125**, 137701 (2020).
[40]A. J. Hoff, *Advanced EPR: Applications in Biology and Biochemistry* (Elsevier, 1989).
[41]J. Köhler, "Magnetic resonance of a single molecular spin," Phys. Rep. **310**, 261 (1999).
[42]S. Lloyd, "Enhanced sensitivity of photodetection via quantum illumination," Science **321**, 1463 (2008).
[43]S. Koenig, D. Lopez-Diaz, J. Antes, F. Boes, R. Henneberger, A. Leuther, A. Tessmann, R. Schmogrow, D. Hillerkuss, R. Palmer, T. Zwick, C. Koos, W. Freude, O. Ambacher, J. Leuthold, and I. Kallfass, "Wireless sub-THz communication system with high data rate," Nat. Photonics **7**, 977 (2013).
[44]I. Pastor-Marazuela, L. Connor, J. van Leeuwen, Y. Maan, S. ter Veen, A. Bilous, L. Oostrum, E. Petroff, S. Straal, D. Vohl, J. Attema, O. M. Boersma, E. Kooistra, D. van der Schuur, A. Sclocco, R. Smits, E. A. K. Adams, B. Adebahr, W. J. G. de Blok, A. H. W. M. Coolen, S. Damstra, H. Dénes, K. M. Hess, T. van der Hulst, B. Hut, V. M. Ivashina, A. Kutkin, G. M. Loose, D. M. Lucero, Á. Mika, V. A. Moss, H. Mulder, M. J. Norden, T. Oosterloo, E. Orrú, M. Ruiter, and S. J. Wijnholds, "Chromatic periodic activity down to 120 megahertz in a fast radio burst," Nature **596**, 505 (2021).
[45]D. A. Anderson, E. Paradis, G. Raithel, R. E. Sapiro, and C. L. Holloway, "High-resolution antenna near-field imaging and sub-THz measurements with a small atomic vapor-cell sensing element," in *11th Global Symposium on Millimeter Waves (GSMM)* (IEEE, 2018).
[46]H. Kraus, V. A. Soltamov, D. Riedel, S. Väth, F. Fuchs, A. Sperlich, P. G. Baranov, V. Dyakonov, and G. V. Astakhov, "Room-temperature quantum microwave emitters based on spin defects in silicon carbide," Nat. Phys. **10**, 157 (2014).
[47]M. Fischer, A. Sperlich, H. Kraus, T. Ohshima, G. V. Astakhov, and V. Dyakonov, "Highly efficient optical pumping of spin defects in silicon carbide for stimulated microwave emission," Phys. Rev. Appl. **9**, 054006 (2018).
[48]A. Gottscholl, M. Kianinia, V. Soltamov, S. Orlinskii, G. Mamin, C. Bradac, C. Kasper, K. Krambrock, A. Sperlich, M. Toth *et al.*, "Initialization and read-out of intrinsic spin defects in a van der Waals crystal at room temperature," Nat. Mater. **19**, 540 (2020).
[49]D. M. Arroo, N. M. Alford, and J. D. Breeze, "Perspective on room-temperature solid-state masers," Appl. Phys. Lett. **119**, 140502 (2021).
[50]J. D. Breeze, E. Salvadori, J. Sathian, N. M. Alford, and C. W. M. Kay, "Continuous-wave room-temperature diamond maser," Nature **555**, 493 (2018).
[51]L. Jin, M. Pfender, N. Aslam, P. Neumann, S. Yang, J. Wrachtrup, and R.-B. Liu, "Proposal for a room-temperature diamond maser," Nat. Commun. **6**, 8251 (2015).
[52]H. Wu, X. Xie, W. Ng, S. Mehanna, Y. Li, M. Attwood, and M. Oxborrow, "Room-temperature quasi-continuous-wave pentacene maser pumped by an invasive Ce : YAG luminescent concentrator," Phys. Rev. Appl. **14**, 064017 (2020).
[53]H. J. Carmichael and M. O. Scully, *Statistical Methods in Quantum Optics 1: Master Equations and Fokker-Planck Equations* (Springer, 2014).